

An Artificial Neural Network for Inferring Solar Wind Proxies at Mars

Suranga Ruhunusiri¹, J. S. Halekas¹, J. R. Espley², F. Eparvier³, D. Brain³,
C. Mazelle⁴, Y. Harada⁵, G. A. DiBraccio², Y. Dong³, Y. Ma⁶, E. M. B.
Thiemann³, D. L. Mitchell⁷, and B. M. Jakosky³.

Suranga Ruhunusiri, suranga-ruhunusiri@uiowa.edu

¹Department of Physics and Astronomy,

The University of Iowa, Iowa City, Iowa,

USA.

²NASA Goddard Space Flight Center,

Greenbelt, Maryland, USA.

³Laboratory for Atmospheric and Space

Physics, University of Colorado, Boulder,

Colorado, USA.

⁴IRAP, CNRS, University of Toulouse,

UPS, CNES, France.

⁵Kyoto University, Kyoto, Japan.

This article has been accepted for publication and undergone full peer review but has not been through the copyediting, typesetting, pagination and proofreading process, which may lead to differences between this version and the Version of Record. Please cite this article as doi: 10.1029/2018GL079282

We present a novel method to determine solar wind proxies from sheath measurements at Mars. Specifically, we develop an artificial neural network to simultaneously infer seven solar wind proxies: ion density, ion speed, ion temperature, interplanetary magnetic field magnitude and its vector components, using spacecraft measurements of ion moments, magnetic field magnitude, magnetic field components in the sheath and the solar EUV flux. The ANN was trained and tested using three years of data from the MAVEN spacecraft. When compared with MAVEN's in situ measured values of the solar wind parameters, we find that the ANN proxies for the solar wind ion density, ion speed, ion temperature and interplanetary magnetic field magnitude have percentage differences of 50% or less for 84.4%, 99.9%, 86.8%, and 79.8% of the instances, respectively. For the cone angle and clock angle proxies, 69.1% and 53.3% of instances, respectively, have angle differences of 30° or less.

Keypoints:

- An artificial neural network (ANN) is implemented to infer solar wind proxies from sheath measurements at Mars.

⁶Department of Earth Planetary and Space Sciences, UCLA, Los Angeles, CA, USA.

⁷Space Sciences Laboratory, University of California, Berkeley, California, USA.

- The ANN can determine solar wind ion density, speed, temperature, and magnetic field magnitude with high accuracies.
- The ANN can determine the magnetic field cone and the clock angles with moderate accuracies.

Accepted Article

1. Introduction

1.1. Need for measuring solar wind parameters

In situ observations by Phobos-2, Mars Global Surveyor (MGS), Mars Express (MEX), and recently by the MAVEN spacecraft have revealed that solar wind parameters, typically referred to as solar wind drivers, influence plasma boundary locations, sheath ion moments, turbulence, and atmospheric escape at Mars. Moreover, organizing observations in the Mars plasma environment based on upstream parameters enables to discover whether certain phenomena are influenced by the upstream drivers. Thus, direct measurement of solar wind parameters or deriving their proxies are crucial for investigating plasma environment dynamics at Mars. The objective of this paper is to develop a novel method of deriving solar wind proxies at Mars by using an artificial neural network and in situ measurements of magnetosheath parameters made by the MAVEN spacecraft. Before describing our method, below, we will first describe how the Mars plasma environment is influenced by the solar wind drivers to emphasize the need for direct measurement or deriving solar wind proxies at Mars.

The bow shock location at Mars is influenced by the upstream parameters such as convection electric field direction, magnetic field orientation, Mach number, dynamic pressure, and EUV flux. The bow shock tends to be located at a larger distance in the hemisphere in the direction of the upstream convection electric field [Dubinin *et al.*, 1998]. The quasi-perpendicular bow shock tends to lie farther upstream than the quasi-parallel bow shock [Dubinin *et al.*, 1998; Halekas *et al.*, 2017b]. The bow shock location lies much closer to the planet during the times of high Mach number [Edberg *et al.*, 2010; Halekas *et al.*, 2017a] and dynamic pressure [Edberg *et al.*, 2009; Halekas *et al.*, 2017a; Hall *et al.*, 2016].

However, the bow shock is found to lie much farther upstream during the times of high EUV flux [Edberg *et al.*, 2009; Halekas *et al.*, 2017a; Hall *et al.*, 2016]. The magnetic pileup boundary (MPB) is also influenced by the upstream parameters [Brain *et al.*, 2005; Edberg *et al.*, 2008, 2009].

Ion temperature and its anisotropy in the sheath and the foreshock are influenced by the upstream magnetic field orientation and Mach number [Halekas *et al.*, 2017b]. Parallel temperature has larger values in the quasi-parallel flank than in the quasi-perpendicular flank, whereas the perpendicular temperature has approximately the same values in both the quasi-parallel and quasi-perpendicular flanks. Thus, the temperature anisotropy tends to be much larger in the quasi-perpendicular flank than in the quasi-parallel flank. Under high Mach numbers, both the parallel and perpendicular temperatures have been found to increase. However, the ion temperature anisotropy has been found to be higher for low Mach numbers than for high Mach numbers.

Waves and turbulence at Mars are affected by the EUV flux, upstream convection electric field, magnetic field orientation, Mach number, and proton beta. Low-frequency waves and turbulence levels are enhanced during the times of high EUV flux [Romanelli *et al.*, 2016; Ruhunusiri *et al.*, 2017, 2018a]. The waves and turbulence show asymmetries with respect to the upstream convection electric field direction and in the quasi-parallel vs. quasi-perpendicular foreshock regions and the adjacent sheath regions [Wei *et al.*, 2006; Ruhunusiri *et al.*, 2017; Fowler *et al.*, 2017]. Mach number and proton beta have also been found to influence wave occurrence rates of waves such as the 1 Hz waves [Ruhunusiri *et al.*, 2018a].

Atmospheric loss via acceleration of heavy ions is influenced by the upstream convection electric field [Dubinin *et al.*, 2011; Johnson *et al.*, 2018]. Acceleration of ions via the convection electric field together with the large ion gyro-radius effects lead to asymmetries in the heavy ion distribution in the Mars plasma environment [Fang *et al.*, 2008; Jarvinen *et al.*, 2015; Dong *et al.*, 2017]. Ion escape has also been found to be sensitive to the EUV flux variation at Mars [Dong *et al.*, 2017]. Ion escapes have been observed to be enhanced during upstream impulsive events such as coronal mass ejections suggesting that increase in solar wind fluxes lead to enhanced ion loss [Edberg *et al.*, 2010; Futaana *et al.*, 2008; Jakosky *et al.*, 2015]. Unraveling how the upstream parameters influence the atmospheric escape is crucial to extrapolating Mars' atmospheric escape backward in time to determine the total atmospheric mass lost to space [Lillis *et al.*, 2015].

Organizing the observations with the upstream parameters is necessary to determine how the Mars plasma environment phenomena are influenced by them. For example, investigators typically organize observations in the Mars Solar Electric coordinates system (MSE) where X-axis is aligned with the solar wind velocity, Y-axis is aligned with the magnetic field component perpendicular to the solar wind velocity and Z-axis is aligned with the convection electric field direction. Dong *et al.* [2015], for example, used MSE coordinate system to organize ion flux observations at Mars, which enabled them to characterize the contributions from different escape channels such as tail vs. plume.

1.2. Previous methods for determining solar wind proxies at Mars

Since Mars lacks a dedicated solar wind monitor, the above-described discoveries were made using a derivation of solar wind proxies at Mars. We will describe three most com-

monly used methods below. The first method is extrapolating solar wind measurements at Earth to Mars. The second method is interpolating two successive measurements made by the orbital assets when they are located upstream of the bow shock. The third method is to use a physics-based model to infer upstream parameters using spacecraft in-situ measurements of the downstream parameters.

In the method of extrapolation, the solar wind parameters measured at earth are appropriately scaled considering how these parameters vary with the heliocentric distance [Edberg *et al.*, 2010]. For example, the solar wind density and magnetic field magnitude have a $1/r^2$ dependence and the solar wind ion temperature has a $1/r^{2/3}$ dependence with heliocentric distance r . However, this method can be utilized only when Mars and Earth are located in approximately the same solar wind sector. Comparing the extrapolated solar wind bulk velocities measurements from STEREO A and B to in-situ measurements made by Mars Express, Opitz *et al.* [2010] suggested that a reliable estimation can only be made when the longitudinal separation between Earth and Mars is less than 65° . Thus, the use of this method to derive solar wind proxies at Mars is limited to typically a couple of months every 2 years.

The second method is to interpolate two adjacent measurements of a solar wind parameter made by a spacecraft when it is in the solar wind to determine the corresponding value of that parameter when the spacecraft is located downstream of the bow shock. For example, MAVEN spacecraft periodically ventures into the solar wind when its apoapsis is located outside Mars' bow shock. So, when the spacecraft is located downstream of the bow shock, in order to infer the solar wind proxies, first two adjacent measurements of the

solar wind parameters are linearly interpolated. Then, it is assumed that the interpolated value is equal to the value of the solar wind parameter of interest. Alternatively, one can assume that a solar wind proxy for a parameter is equal to its most recent measurement made when the spacecraft was located upstream of the bow shock. A statistical study of the solar wind parameters using the MAVEN spacecraft measurements has revealed that this latter approximation is suitable as long as the time duration is less than or equal to about a couple of hours [Marquette *et al.*, 2018]. Implementation of these techniques is not possible during the times when the spacecraft does not have upstream solar wind coverage due to a precession of the orbit.

In the third approach, certain solar wind parameters are inferred based on the spacecraft measurements of the downstream parameters using a physics-based model. For example, assuming that the magnetic field pressure in the MPB balances the incident solar wind dynamic pressure, the upstream solar wind dynamic pressure can be inferred based on magnetic field measurements in the MPB [Crider *et al.*, 2003].

Alternatively, two spacecraft measurements can be used to obtain direct measurements of the solar wind in the absence of a dedicated monitor. When one spacecraft is located downstream of the bow shock, if a second spacecraft is simultaneously located upstream of the bow shock, the measurements of the second spacecraft in the solar wind can be used to determine the solar wind parameters corresponding to the times when the first spacecraft was located downstream of the bow shock. This method has recently been used by the MEX and MAVEN spacecraft [Harada *et al.*, 2018]. However, this ideally works if two spacecraft have identical instruments. While Mars currently has six orbiters, they all

do not have identical plasma instruments. For example, while the MAVEN spacecraft has a magnetometer the MEX lacks a magnetometer. Thus, interplanetary magnetic field can only be obtained for times when MAVEN ventures upstream of the bow shock. Recent studies have also utilized MHD models to derive solar wind proxies at Mars [Fang *et al.*, 2018; Ma *et al.*, 2018].

The influence of upstream parameters on the Mars plasma environment dynamics and the need for these parameters for organizing downstream observations, as we discussed in the previous section, emphasize the need for continuous solar wind monitoring or developing techniques to derive solar wind proxies that are complementary to existing methods that we discussed above. In this paper, we introduce a novel method to infer solar wind proxies at Mars. We, in particular, develop an artificial neural network to infer solar wind proxies using MAVEN particle and field measurements in the sheath. This is the first time that an artificial neural network has been employed to derive solar wind proxies at any planet. This is also the first time that an artificial neural network has been used for an application involving plasma observations at Mars. The combination of our method for deriving solar wind proxies using MAVEN spacecraft observations in the sheath with its direct measurements of the solar wind parameters will enable to provide solar wind proxies for majority of times from September of 2014 onwards. Thus, this work should be of interest to a large scientific community who are involved in investigating the impact of the upstream drivers on the Mars plasma environment. The methods developed in this paper should also be of interest to the planetary-physics and heliospheric scientific communities.

1.3. Artificial Neural Networks

Here, we briefly introduce artificial neural networks (ANNs) and their applications. Artificial neural networks consist of computational units called neurons which are analogous to the biological neurons [Samarasinghe, 2007]. A neuron consists of one or more inputs and outputs. The neuron computes a weighted sum of its inputs (and also applies a bias to this weighted sum). Then, it produces an output using a transfer function which can be either linear or nonlinear. A typical ANN contains hundreds of such neurons. The number of inputs, outputs, and transfer functions of the neurons in the ANN must be user specified. The ANN determines the weights and biases during a process called training by comparing the outputs it produces, for a set of inputs provided by the user, to a set of targets also provided by the user.

Artificial Neural Networks are powerful at identification of patterns in the observational data analogous to their biological counterparts. Thus, artificial neural networks have been successfully used in a variety of applications in many fields such as hydrology [Hsu *et al.*, 1995], chemostratigraphy [Malmgren and Nordlund, 1996], climatology [Jiang *et al.*, 2018], seismology [Dai *et al.*, 1997], and cosmology [George and Huerta, 2018]. Applications of ANNs in space physics include Earth's magnetospheric response and parameter prediction [Chu *et al.*, 2017a, b; Gleisner and Lundstedt, 1997], ionospheric parameter prediction [Tulunay *et al.*, 2006], and plasma wave identification [Ruhunusiri *et al.*, 2018b]. In this paper, we will describe the development of an ANN to derive solar wind proxies at Mars.

2. Method

Our overall approach was to develop an ANN that can simultaneously infer seven solar wind proxies: solar wind ion density, ion speed, ion temperature, interplanetary magnetic field (IMF) magnitude, and its three vector components. As we discussed in Sec. 1.1, there is an interrelation between sheath ion moments and magnetic field to the solar wind ion moments, interplanetary magnetic field, and EUV flux and these interrelations also generally depend on the spatial location within the Mars plasma environment. Thus, we used following inputs to the ANN: magnetosheath location, magnetosheath ion density, ion speed, ion temperature, magnetic field magnitude, magnetic field components, and EUV flux. Since the dependencies of the sheath parameters to the solar wind parameters may not be necessarily linear, we used nonlinear elements in the ANN such as nonlinear transfer functions.

2.1. ANN architecture

We used a feedforward neural network [Beale *et al.*, 2010] with eleven inputs, a normalization layer, two hidden layers, an output layer, a denormalization layer, and seven outputs (see Figure 1). Similar neural network architectures have been successfully used in nonlinear regression applications [Rojas, 1996]. The inputs are the spacecraft location in cylindrical coordinates (X_{MSO} , R_{MSO} , and $\theta = \tan^{-1}(Y_{MSO}/Z_{MSO})$ where MSO stands for Mars Solar Orbital coordinate system), the magnetosheath ion density, ion speed, ion temperature, magnetic field magnitude, magnetic field components (in MSO coordinates), and the EUV flux. A normalization layer was used to normalize the input values between -1 and +1. The first hidden layer contains 24 neurons each with a hyperbolic tangent

sigmoid (tansig) transfer function which is a standard nonlinear function used in neural networks and this has the form $2/(1 + e^{-2n}) - 1$ where $n = \Sigma(I_i \cdot w_i + b_i)$. Here, I_i are the input values, w_i are the weights, and b_i are the bias values. The reason for normalization of the inputs to the range -1 and 1 is that the output of the tansig transfer function reaches limiting values of -1 and 1 for n values less than -1 and greater than 1, respectively. The second hidden layer contains 12 neurons each also with tansig transfer functions. The output layer contains seven neurons each with a linear transfer function of the form $y = x$ where y is the output of a neuron and x is the input to a neuron. The outputs from the output layer are then denormalized by the denormalization layer to scale the parameters to the realistic range of values. Finally, the ANN produces seven outputs: solar wind ion density, ion speed, ion temperature, IMF magnitude, and IMF components.

The ANN for solar wind inference was constructed, trained, validated, and tested using the MATLAB neural network toolbox [Demuth, 2002; Beale et al., 2010]. We will describe the data selection, ANN training, validation, and testing procedures below. Training and validation were used to train the network and to select the best architecture. Testing was used to determine the ability of the network to infer the solar wind parameters from sheath measurements.

2.2. Data selection

To perform ANN training, validation, and testing, we require sheath parameters and solar wind parameters corresponding to the times where the sheath parameter measurements were made so that during training the ANN can learn the relationships between the sheath parameters and the solar wind parameters. We selected 3 years of MAVEN space-

craft data spanning from December 1, 2014 to January 31, 2018 to perform ANN training, validation, and testing. Whether the spacecraft was in the solar wind was determined using an automated procedure described in Sec. 3.1 of [Halekas *et al.*, 2017a]. When the spacecraft was determined to be in the solar wind, an orbit average of the solar wind parameters was determined for each orbit. We used the Solar Wind Ion Analyzer (SWIA) instrument [Halekas *et al.*, 2015, 2017a] measurements to determine the solar wind ion moments (density, speed, and temperature) and the magnetometer (MAG) [Connerney *et al.*, 2015a, b] to obtain the IMF components. The distribution of the measured solar wind ion moments and IMF magnitude and orientations (clock and cone angles) are depicted in Figure 2. Time segments where the spacecraft was traversing through the sheath was identified by determining whether the spacecraft was located between the nominal bow shock and the magnetic pileup boundary using the boundary models by Trotignon *et al.* [2006]. Then, 4-minute averages of the sheath ion moments (determined using the SWIA instrument) and magnetic field magnitudes and its components (determined using the MAG instrument) were computed to obtain average sheath parameters to minimize the effects of turbulent fluctuations in the sheath. Then, for each of the locations in the sheath, we determined the corresponding solar wind parameters by assuming that they are equal to the value of the temporally closest measurements of the two adjacent solar wind measurements. We required that the temporally closest measurement of the solar wind parameter should be available within a temporal separation of less than 2 hours. Otherwise, both the sheath parameters and the corresponding solar wind parameters were removed from the dataset. We used the Lyman-alpha flux measured by the EUV monitor

[Eparvier et al., 2015] onboard the MAVEN spacecraft as an input to the ANN which is a proxy for the EUV flux.

2.3. ANN training, validation, and testing

We used 80% of the data for training and validation and the remaining 20% of the data for testing as typically done for ANNs after randomizing the data. The sheath parameters were used as the inputs to the ANN while the solar wind parameters were used as targets. The ANN was trained using the resilient backpropagation algorithm [Riedmiller and Braun, 1993] which determines the weights and biases of the neurons minimizing the difference between network outputs and targets. We selected this algorithm because it yielded fast convergence times while producing high accuracies.

A 10-fold cross validation [Rudy Setiono, 2001] was performed using the training and validation data set to obtain the best ANN architecture containing 24 neurons in the first hidden layer and 12 neurons in the second hidden layer that we discussed in Sec 2.1. When the network complexity is lower, for example, ANNs consisting of lower than 24 neurons in the first hidden layer and less than 12 neurons in the second layer, the accuracies are lower. For more complex architectures, for example, ANNs consisting of more than 24 neurons in the first hidden layer and more than 12 neurons in the second hidden layer, the network accuracies do not significantly improve compared to the one with 24 and 12 neurons in the first and second hidden layers. Also, as the complexity of the ANN architecture is increased, the network training time increases and the ANN tends to memorize the relationships between the inputs and targets rather than generalizing the relationships between them [Samarasinghe, 2007]. Thus, we selected the ANN with 24

neurons in the first hidden layer and 12 neurons in the second hidden layer as the optimum ANN architecture for deriving solar wind proxies using sheath measurements.

After selection of the optimum network architecture, the testing dataset was used to assess the accuracies of the ANN. A comparison of the measured solar wind parameters and ANN inferred solar wind proxies for a five-day period in the testing dataset is depicted in Figure 3. The ANN inference accuracies and uncertainties associated with those inferences, determined using the entire testing dataset, are depicted in Figure 4 (See Figure S1 in the supporting material for the corresponding parameters for an ANN trained and tested using 70% and 30% of data, respectively). The uncertainties shown in Figure 4 are the 50% and 75% confidence intervals for the absolute difference between the ANN estimates based on the 4-minute averaged sheath values and the corresponding orbit-averaged values of the solar wind parameters.

3. Results and Discussions

We find that the ANN can infer the solar wind ion density, ion speed, ion temperature, and magnetic field magnitude with high accuracies and the clock angle and the cone angle with moderate accuracies. Figure 3 depicts a comparison of the measured solar wind parameters and the ANN solar wind proxies for a five-day period. Note that Figure 3 depicts the orbit-average values of the measured upstream values and the ANN predicted values. For the time period shown in Figure 3, for a majority of times, the ANN solar wind proxies lie within a factor of two of the solar wind measurements.

In order to assess the overall performance of the ANN, we computed the accuracies of the ANN solar wind proxies using the entire testing dataset. For ion moment and

the magnetic field magnitude ANN proxies, we computed the percentage differences as a measure of their accuracies where percentage difference = $| \text{ANN proxy} - \text{Measured value} | \times 100 / (\text{Measured value})$ while for the magnetic field cone and clock angle ANN proxies, we computed the difference between the ANN proxy values and the measured values as a measure of the angle accuracies. The histograms of these percentage differences and angle differences for the ANN solar wind proxies are shown in Figure 4. The percentage of instances where the ANN proxies for the solar wind ion density, ion speed, ion temperature, and IMF magnitude have percentage differences of 50% or less are 84.4%, 99.9%, 86.8%, and 79.8%, respectively. For the cone angle and clock angle proxies, 69.1% and 53.3% of instances, respectively, have angle differences of 30° or less. Thus, accuracies are highest for the ANN solar wind ion speed proxies followed by ion density, temperature, and IMF magnitude proxies. Accuracies for ANN cone angle proxies are higher than those for the clock angle proxies.

To determine the uncertainties associated with the ANN proxies, we plot confidence interval plots in Figure 4. The x-axis in these confidence interval plots depict the ANN proxy value and the two shaded regions show where the uncertainties have 50% and 75% probabilities of being less than the upper boundary value of these regions. For example, if the ANN solar wind ion density proxy value is 6 cm^{-3} , there is a 50% probability that the uncertainty is less than 1.1 cm^{-3} and a 75% probability that the uncertainty is less than 2.1 cm^{-3} (see Figure 4b).

The ANN proxies have small uncertainties for values where they occur with a high percentage in the solar wind. For example 94% of the time, the solar wind ion density is

less than 8cm^{-3} and the remaining 6% of the times it has values greater than 8cm^{-3} as can be seen in Figure 2(a) and the ANN solar wind ion density proxy values have uncertainties of typically 1cm^{-3} for values less than 8cm^{-3} (here we determine the typical uncertainty using the 75% confidence interval for the uncertainty shown in Figure 4(b)), whereas the uncertainties are larger, typically 3.5cm^{-3} , when the ANN proxy value is above 8cm^{-3} .

If we consider another example, the uncertainties for the ANN proxies for the IMF clock angles are small near 90° and 270° as can be seen in Figure 4(l). As can be seen in Figure 2(k), these clock angles occur with a high percentage in the solar wind. Thus, the larger uncertainty associated with values that occur with a lower probability in the solar wind should be a consequence of the ANN not being able to sufficiently learn the relationships between the sheath parameters and the solar wind parameters for those range of values.

However, as the MAVEN mission progresses, we will have more data to train the ANN. So, the network performance can be improved even further with the use of more data.

The sheath parameters are sensitive to variability on sub-orbit timescales to the upstream parameters and this is not captured in the training data set as we used orbit averaged values for the upstream parameters to train and test the ANN. Consequently, the uncertainties shown in Figure 4 do not include the uncertainties arising from the sub-orbit variation of the upstream parameters. However, if orbit-averaged ANN inferred values are used as shown in Figure 3 instead of the ANN inferred values based on the 4-minute averaged sheath values, the uncertainties shown in Figure 4 can be considered as worst-case limits (see Figure S2 in the supporting material).

The reader may be curious as to why the magnetic field magnitude and its three components were used as inputs to the ANN instead of merely the three components of the magnetic field or the magnetic field magnitude, cone angle, and the clock angle. The reason for this is that, during preliminary training and testing of ANNs using the latter mentioned input combinations, we found that the ANN inferred accuracies for the IMF magnitude, clock angle, and the cone angle are much lower than those of the ANN that used the magnetic field magnitude and its three components as inputs (see Figure S3 in the supporting material).

4. Summary

We developed an ANN to infer solar wind proxies using sheath measurements. The ANN was trained, validated, and tested using MAVEN data spanning 3 years. The ANN can simultaneously infer seven solar wind parameters: ion density, ion speed, ion temperature, magnetic field magnitude and its three components using the corresponding measurements in the sheath and the EUV flux. We find that the ANN has very good accuracies for the ion moment and magnetic field magnitude inferences and moderate accuracies for magnetic field orientation inferences. We also find that the ANN proxies have small uncertainties for values that occur with larger probability in the solar wind than those value that occur with lower probability. Combining the ANN proxies of the solar wind with the measured values by the MAVEN spacecraft enables to provide a solar wind dataset at Mars for a majority of times from September of 2014 onwards which should be invaluable to numerous investigators who are involved in studying the response

of the Mars plasma environment to the solar wind drivers. The techniques developed here should also be of interest to the planetary physics and heliospheric scientific communities.

Acknowledgments. This work was supported by NASA. C. Mazelle was supported by CNES. We thank J. E. P. Connerney for MAG data. MAVEN data are publicly available through the Planetary Data System.

References

- Beale, M. H., M. T. Hagan, and H. B. Demuth (2010), *Neural Network Toolbox 7: User's Guide*, Natick, MA: The Math Works, Inc.
- Brain, D. A., J. S. Halekas, R. Lillis, D. L. Mitchell, R. P. Lin, and D. H. Crider (2005), Variability of the altitude of the Martian sheath, *Geophys. Res. Lett.*, 32, L18203, doi: 10.1029/2005GL023126.
- Chu, X. N., J. Bortnik, W. Li, Q. Ma, V. Angelopoulos, and R. M. Thorne (2017a), Erosion and refilling of the plasmasphere during a geomagnetic storm modeled by a neural network, *J. Geophys. Res. Space Physics*, 122, 7118-7129, doi: 10.1002/2017JA023948.
- Chu, X., et al. (2017b), A neural network model of three-dimensional dynamic electron density in the inner magnetosphere, *J. Geophys. Res. Space Physics*, 122, 9183-9197, doi: 10.1002/2017JA024464.
- Connerney, J., J. Espley, P. Lawton, S. Murphy, J. Odom, R. Oliverson, and D. Shepard (2015a), The MAVEN Magnetic Field Investigation, *Space Sci. Rev.*, 1-35, doi:10.1007/s11214-015-0169-4.

Connerney, J. E. P., J. R. Espley, G. A. DiBraccio, J. R. Gruesbeck, R. J. Oliverson, D. L. Mitchell, J. Halekas, C. Mazelle, D. Brain, and B. M. Jakosky (2015b), First results of the MAVEN magnetic field investigation, *Geophys. Res. Lett.*, *42*, 8819-8827, doi:10.1002/2015GL065366.

Crider, D. H., D. Vignes, A. M. Krymskii, T. K. Breus, N. F. Ness, D. L. Mitchell, J. A. Slavin, and M. H. Acuña (2003), A proxy for determining solar wind dynamic pressure at Mars using Mars Global Surveyor data, *J. Geophys. Res.*, *108*, 1461, doi: 10.1029/2003JA009875, A12.

Dai, H. and C. MacBeth (1997), The application of back-propagation neural network to automatic picking seismic arrivals from single-component recordings, *J. Geophys. Res.*, *102*(B7), 15105-15113, doi: 10.1029/97JB00625.

Demuth, H. and M. Beale, (2002), *Neural Network Toolbox: For Use with MATLAB*, Natick, MA: The Math Works, Inc.

Dong, Y., X. Fang, D. A. Brain, J. P. McFadden, J. S. Halekas, J. E. Connerney, S. M. Curry, Y. Harada, J. G. Luhmann, and B. M. Jakosky (2015), Strong plume fluxes at Mars observed by MAVEN: An important planetary ion escape channel, *Geophys. Res. Lett.*, *42*, 8942-8950, doi: 10.1002/2015GL065346.

Dong, Y., X. Fang, D. A. Brain, J. P. McFadden, J. S. Halekas, J. E. P. Connerney, F. Eparvier, L. Andersson, D. Mitchell, and B. M. Jakosky (2017), Seasonal variability of Martian ion escape through the plume and tail from MAVEN observations, *J. Geophys. Res. Space Physics*, *122*, 4009-4022, doi: 10.1002/2016JA023517.

Dubinin, E., K. Sauer, M. Delva, and T. Tanaka (1998), The IMF control of the Martian bow shock and plasma flow in the magnetosheath. Predictions of 3 – *D* simulations and observations. *Earth, Planets, and Space*, 50(10), 873-882, <https://doi.org/10.1186/BF03352181>.

Dubinin, E., M. Fraenz, A. Fedorov et al. (2011), Ion Energization and Escape on Mars and Venus, *Space Sci Rev* 162, 173-211, <https://doi.org/10.1007/s11214-011-9831-7>.

Edberg, N. J. T., M. Lester, S. W. H. Cowley, D. A. Brain, M. Fränz, and S. Barabash (2010), Magnetosonic Mach number effect of the position of the bow shock at Mars in comparison to Venus, *J. Geophys. Res.*, 115, A07203, doi:10.1029/2009JA014998.

Edberg, N. J. T., M. Lester, S. W. H. Cowley, and A. I. Eriksson (2008), Statistical analysis of the location of the Martian magnetic pileup boundary and bow shock and the influence of crustal magnetic fields, *J. Geophys. Res.*, 113, A08206, doi:10.1029/2008JA013096.

Edberg, N. J. T., D. A. Brain, M. Lester, S. W. H. Cowley, R. Modolo, M. Fränz, and S. Barabash (2009), Plasma boundary variability at Mars as observed by Mars Global Surveyor and Mars Express, *Ann. Geophys.*, 27, 3537-3550.

Edberg, N. J. T., H. Nilsson, A. O. Williams, M. Lester, S. E. Milan, S. W. H. Cowley, M. Frnz, S. Barabash, and Y. Futaana (2010), Pumping out the atmosphere of Mars through solar wind pressure pulses, *Geophys. Res. Lett.*, 37, L03107, doi:10.1029/2009GL041814.

Fang, X., M. W. Liemohn, A. F. Nagy, Y. Ma, D. L. De Zeeuw, J. U. Kozyra, and T. H. Zurbuchen (2008), Pickup oxygen ion velocity space and spatial distribution around

Mars, *J. Geophys. Res.*, 113, A02210, doi: 10.1029/2007JA012736.

Fang, X., Ma, Y., Luhmann, J., Dong, Y., Brain, D., Hurley, D., et al. (2018).

The morphology of the solar wind magnetic field draping on the dayside of Mars and its variability. *Geophysical Research Letters*, 45, 33563365. <https://doi-org.proxy.lib.uiowa.edu/10.1002/2018GL077230>

Eparvier, F. G., et al. (2015), The Solar Extreme Ultraviolet Monitor for MAVEN, *Space Sci. Rev.*, 195, 293-301, doi:10.1007/s11214-015-0195-2.

Fowler, C. M., L. Andersson, J. Halekas, J. R. Espley, C. Mazelle, E. R. Coughlin, R. E. Ergun, D. J. Andrews, J. E. P. Connerney, and B. Jakosky (2017), Electric and magnetic variations in the near Mars environment, *J. Geophys. Res. Space Physics*, 122, 8536-8559, doi: 10.1002/2016JA023411.

Futaana, Y., et al. (2008), Mars Express and Venus Express multi-point observations of geoeffective solar flare events in December (2006), *Planet. Space Sci.*, 56, 873-880, doi:10.1016/j.pss.2007.10.014.

Gleisner, H., and H. Lundstedt (1997), Response of the auroral electrojets to the solar wind modeled with neural networks, *J. Geophys. Res.*, 102(A7), 14269-14278, doi: 10.1029/96JA03068.

George, D. and E.A. Huerta,(2018), Deep Learning for real-time gravitational wave detection and parameter estimation: Results with Advanced LIGO data, *Physics Letters B*, 778, 64-70, doi.org/10.1016/j.physletb.2017.12.053.

Halekas, J. S., E. R. Taylor, G. Dalton, G. Johnson, D. W. Curtis, J. P. McFadden, D. L. Mitchell, R. P. Lin, and B. M. Jakosky (2015), The Solar Wind Ion Analyzer for

MAVEN, *Space Sci. Rev.*, doi:10.1007/s11214-013-0029-z.

Halekas, J. S., et al. (2017a), Structure, dynamics, and seasonal variability of the Mars-solar wind interaction: MAVEN Solar Wind Ion Analyzer in-flight performance and science results, *J. Geophys. Res. Space Physics*, 122, 547-578, doi:10.1002/2016JA023167.

Halekas, J. S. et al. (2017b), Flows, fields, and forces in the Mars-solar wind interaction, *J. Geophys. Res. Space Physics*, 122, 11,320-11,341, doi:10.1002/2017JA024772.

Hall, B. E. S., et al. (2016), Annual variations in the Martian bow shock location as observed by the Mars Express mission, *J. Geophys. Res. Space Physics*, 121, 11,474-11,494, doi: 10.1002/2016JA023316.

Harada, Y., D. A. Gurnett, A. Kopf, J. S. Halekas, and S. Ruhunusiri (2018), Ionospheric irregularities at Mars probed by MARSIS topside sounding. *Journal of Geophysical Research: Space Physics*, 123, 1018-1030. <https://doi.org/10.1002/2017JA024913>

Hsu, K., H. V. Gupta, and S. Sorooshian (1995), Artificial Neural Network Modeling of the Rainfall Runoff Process, *Water Resour. Res.*, 31(10), 2517-2530, doi: 10.1029/95WR01955.

Jakosky, B. M., et al. (2015), MAVEN observations of the response of Mars to an interplanetary coronal mass ejection, *Science*, 350, 0210, doi:10.1126/science.aad3443.

Jarvinen, R., D. A. Brain, and J. G. Luhmann (2015), Planetary ion dynamics in the induced magnetospheres of Venus and Mars, *Planet. Space Sci.*, doi:10.1016/j.pss.2015.08.012.

Jiang, G. Q., J. Xu, and J. Wei (2018), A deep learning algorithm of neural network for the parameterization of typhoon-ocean feedback in typhoon forecast models. *Geophysical*

Research Letters, 45. <https://doi.org/10.1002/2018GL077004>

Johnson, B. C., Liemohn, M. W., Fränz, M., Ramstad, R., Stenberg Wieser, G., and Nilsson, H. (2018), Influence of the interplanetary convective electric field on the distribution of heavy pickup ions around Mars. *Journal of Geophysical Research: Space Physics*, 123, 473-484. <https://doi.org/10.1002/2017JA024463>

Lillis, R.J., Brain, D.A., Bougher, S.W. et al. (2015), Characterizing Atmospheric Escape from Mars Today and Through Time, with MAVEN, *Space Sci Rev*, 195, 357-422, doi.org/10.1007/s11214-015-0165-8.

Ma, Y., Fang, X., Halekas, J. S., Xu, S., Russell, C. T., Luhmann, J. G. et al (2018). The Impact and Solar Wind Proxy of the 2017 September ICME Event at Mars. *Geophysical Research Letters*, 45. <https://doi.org/10.1029/2018GL077707>

Malmgren, B. A., and U. Nordlund (1996), Application of artificial neural networks to chemostratigraphy, *Paleoceanography*, 11(4), 505-512, doi: 10.1029/96PA01237.

Marquette, M., Lillis, R. J., Halekas, J. S., Luhmann, J. G., Gruesbeck, J. R., and Espley (2018), Autocorrelation study of solar wind plasma and IMF properties as measured by the MAVEN spacecraft, *Journal of Geophysical Research: Space Physics*, 123. <https://doi.org/10.1002/2018JA025209>.

Opitz, A., A. Fedorov, P. Wurz, K. Szego, J. A. Sauvaud, R. Karrer, A. B. Galvin, S. Barabash, and F. Ipavich (2010), Solar wind bulk velocity throughout the inner heliosphere from multi-spacecraft measurements, *Solar Phys.*, 264, 377-382, [doi:10.1007/s11207-010-9583-7](https://doi.org/10.1007/s11207-010-9583-7).

Riedmiller, M., and H. Braun (1993), A direct adaptive method for faster backpropagation learning: The RPROP algorithm, Proceedings of the IEEE International Conference on Neural Networks,1, 586-591, doi:10.1109/ICNN.1993.298623.

Rojas, R. (1996), Neural Networks: A systematic Introduction, Berlin, Heidelberg, Springer-Verlag.

Romanelli, N., et al. (2016), Proton cyclotron waves occurrence rate upstream from Mars observed by MAVEN: Associated variability of the Martian upper atmosphere, J. Geophys. Res. Space Physics, 121, 11,113-11,128, doi:10.1002/2016JA023270.

Rudy Setiono (2001), Feedforward Neural Network Construction Using Cross Validation, Neural Computation, 13, 2865-2877.

Ruhunusiri, S., et al. (2017), Characterization of turbulence in the Mars plasma environment with MAVEN observations, J. Geophys. Res. Space Physics, 122, 656-674, doi:10.1002/2016JA023456.

Ruhunusiri, S., Halekas, J. S., Espley, J. R., Eparvier, F., Brain, D., Mazelle, C., et al. (2018a), One-hertz waves at Mars: MAVEN observations, Journal of Geophysical Research: Space Physics, 123, doi:10.1029/2017JA024618.

Ruhunusiri, S. (2018b), Identification of Plasma Waves at Saturn Using Convolutional Neural Networks, IEEE Transactions on Plasma Science, 46, doi:10.1109/TPS.2018.2849940.

Samarasinghe, S., (2007), Neural networks for applied sciences and engineering: from fundamentals to complex pattern recognition, Boca Raton, FL: CRC Press.

Trotignon, J., C. Mazelle, C. Bertucci, and M. Acuña (2006), Martian shock and magnetic pileup boundary positions and shapes determined from the Phobos 2 and Mars Global Surveyor data sets, *Planet. Space Sci.*, 54(4), 357-369, doi:10.1016/j.pss.2006.01.003.

Tulunay, E., E. T. Senalp, S. M. Radicella, Y. Tulunay (2006), Forecasting total electron content maps by neural network technique, *Radio Science*, 41, RS4016, doi:10.1029/2005RS003285.

Wei, H. Y., and C. T. Russell (2006), Proton cyclotron waves at Mars: Exosphere structure and evidence for a fast neutral disk, *Geophys. Res. Lett.*, 33, L23103, doi: 10.1029/2006GL026244.

Accepted Article

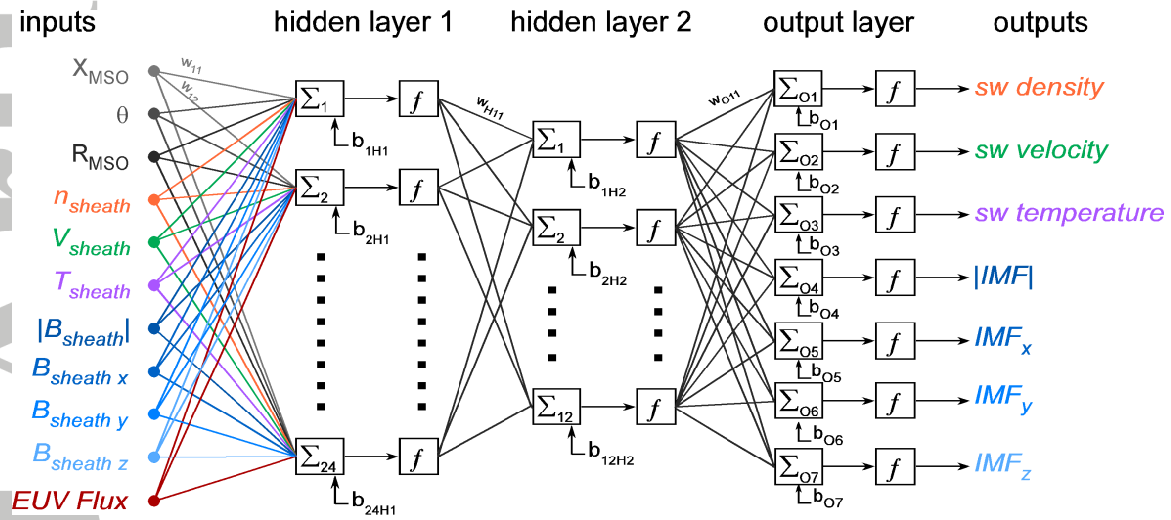


Figure 1. The architecture of the artificial neural network used for inferring solar wind proxies using sheath measurements. The ANN has eleven inputs for spacecraft location, sheath ion moments, magnetic field magnitude and components, and EUV flux and seven outputs for solar wind ion moments and magnetic field magnitude and components. The ANN consists of two hidden layers consisting of 24 and 12 neurons in the first and second hidden layers, respectively. The neurons in the hidden layers have tansig nonlinear transfer functions and the neurons in the output layer have linear transfer functions.

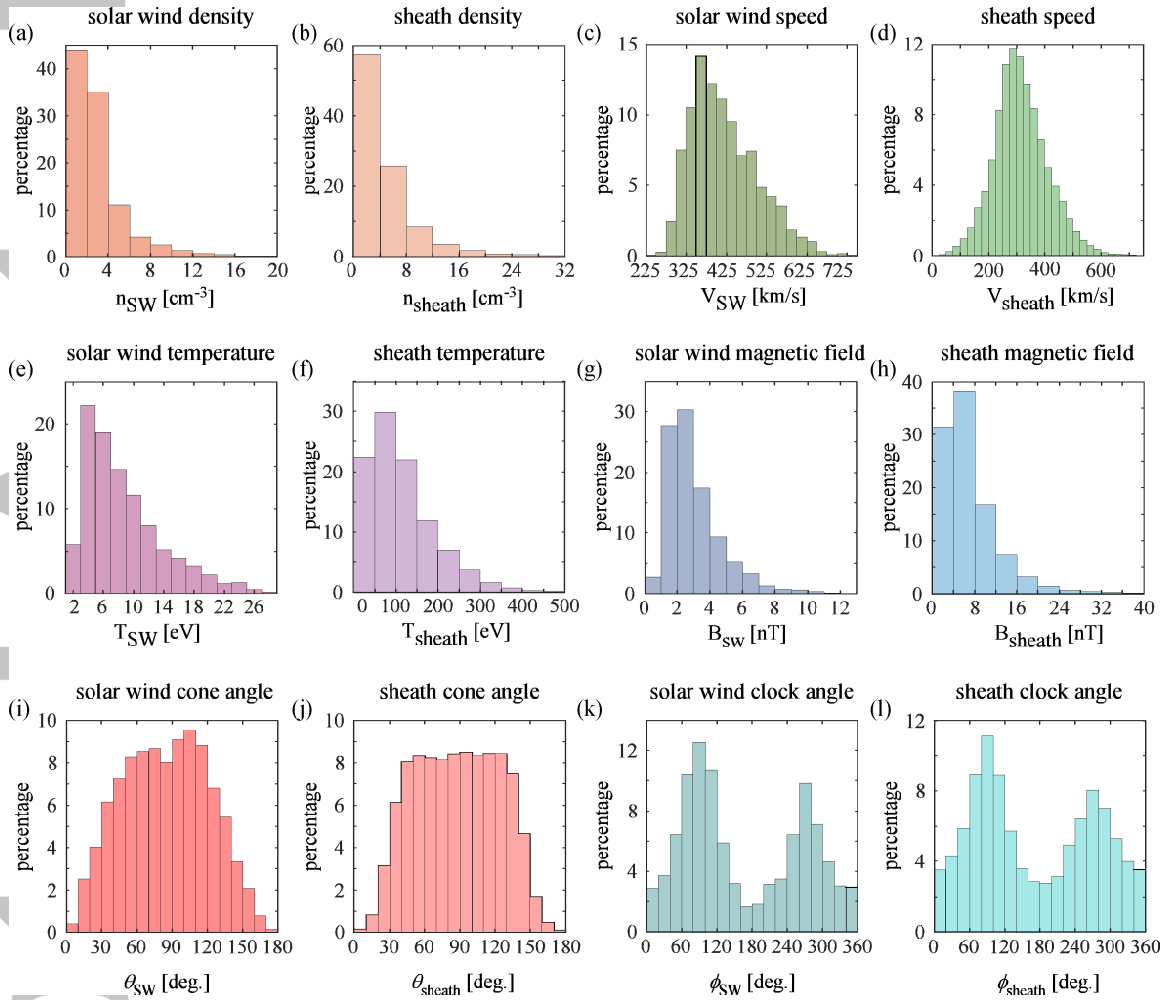


Figure 2. (a),(c),(e),(g),(i),(k) Distributions of the MAVEN measurements of the solar wind ion moments, IMF magnitude and orientations. (b),(d),(f),(h),(j),(l) Distributions of the MAVEN measurements of sheath ion moments, magnetic field magnitude and orientations. Here, n_{SW} , V_{SW} , T_{SW} , B_{SW} , θ_{SW} , and ϕ_{SW} denote solar wind ion density, ion speed, ion temperature, IMF magnitude, IMF cone angle, and IMF clock angle, respectively. These data were used for training, validation, and testing the ANN. Note that different scales are used for plotting the solar wind and sheath ion moments and IMF magnitude. Here cone angle = $\cos^{-1}(B_x/|B|)$ and clock angle = $\tan^{-1}(B_y/B_z)$ where B_x , B_y , B_z are the sheath or IMF magnetic field components in MSO coordinates and $|B|$ is the sheath or IMF magnetic field magnitude. We use the four quadrants in the $B_y - B_z$ plane determined by the signs of B_y and B_z to obtain $0^0 - 360^0$ value range for the clock angle.

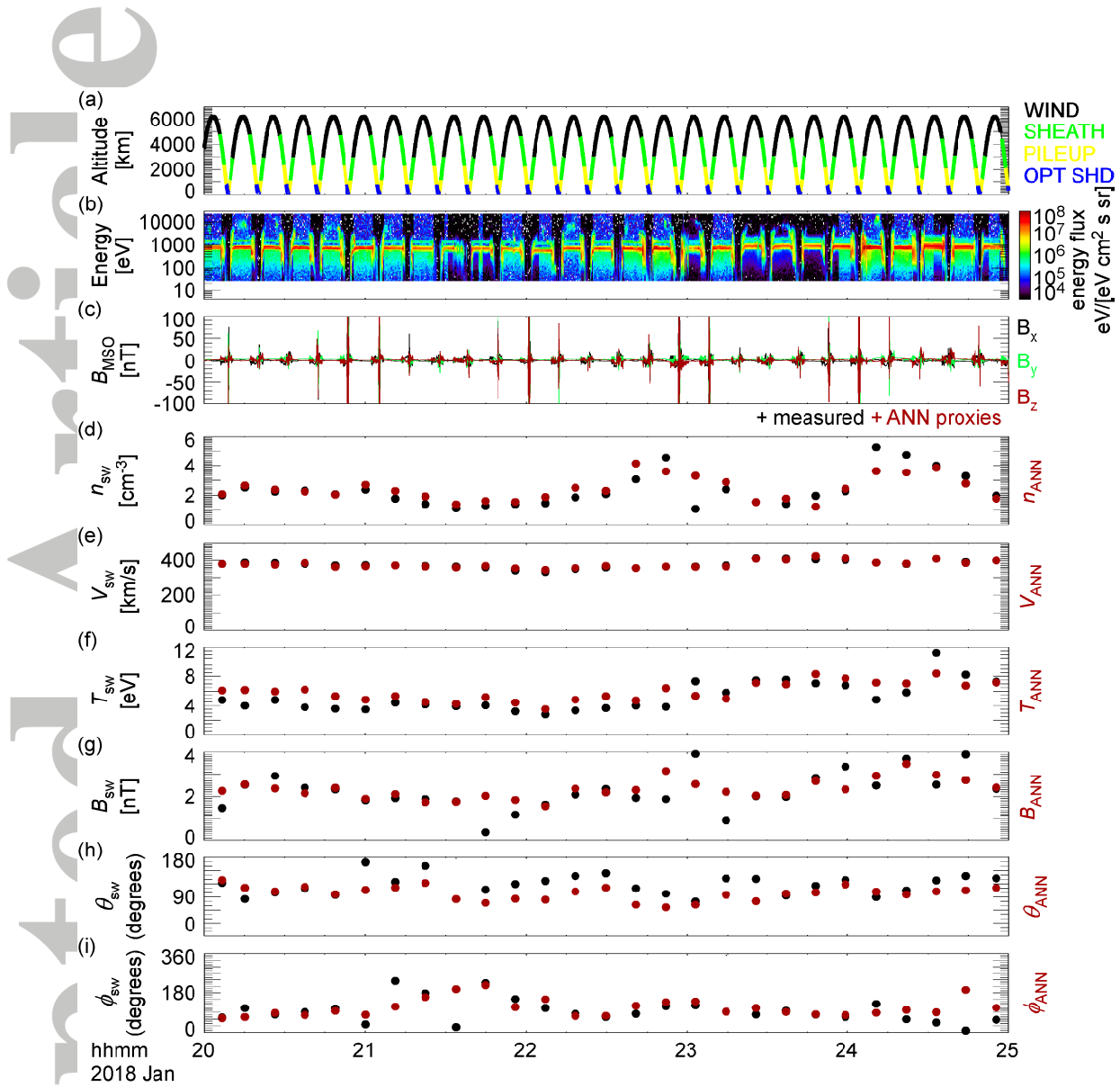


Figure 3. (a) MAVEN spacecraft altitude with a color coding to indicate different regions in the Mars plasma environment. (b) A times stack of ion energy spectra from SWIA instrument which were used to determine the solar wind and sheath ion moments. (c) Time series of the three components of the magnetic field in MSO coordinate system measured by the MAG instrument. (d)-(i) Measured vs. ANN proxies for solar wind ion moments and IMF magnitude and orientations. The measured solar wind values are depicted in black, whereas the ANN proxies are depicted in red. Here, n_{ANN} , V_{ANN} , T_{ANN} , B_{ANN} , θ_{ANN} , and ϕ_{ANN} denote ANN proxies for solar wind ion density, ion speed, ion temperature, IMF magnitude, IMF cone angle, and IMF clock angle, respectively. Each data point represents the orbit averages of the measured solar wind values and the ANN proxy values.

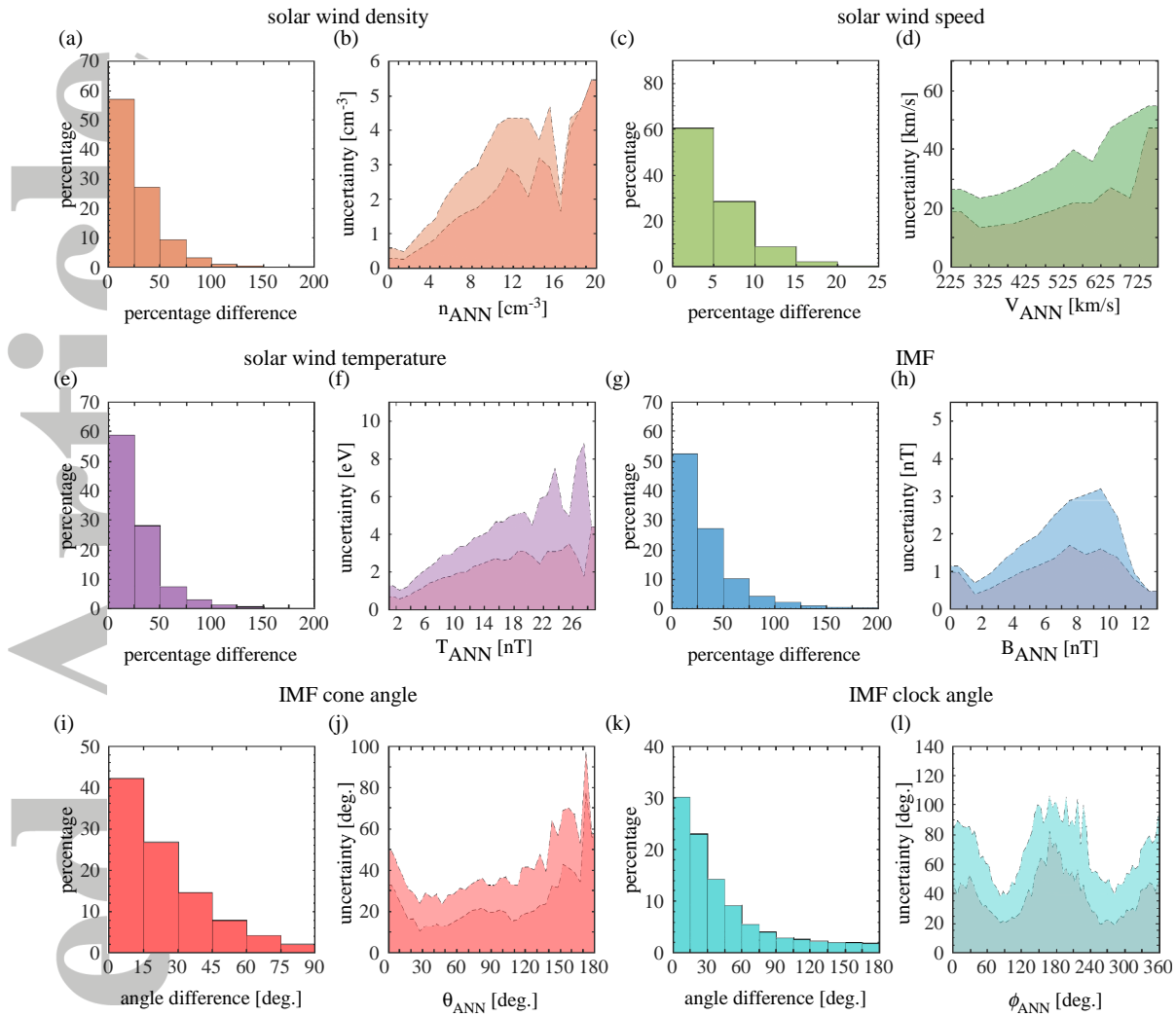


Figure 4. (a)-(h) Histograms for the percentage differences and confidence interval plots of uncertainties for the ANN solar wind ion moment- and IMF magnitude- proxies. (i)-(l) Histograms for angle differences and confidence interval plots of uncertainties for the ANN IMF cone and clock angle proxies. The two shaded regions in panels (b),(d),(f),(h),(j), and (l) depict the 50% and 75% confidence intervals for the uncertainties. The ANN has very good accuracies for solar wind ion moment and IMF magnitude inferences, whereas it has moderate accuracies for IMF cone and clock angle inferences.